A Multilevel Domain Decomposition Approach for Studying Coupled Flow Applications

E. Aulisa[1], A. Cervone[2], S. Manservisi[2] and P. Seshaiyer[3,*]

[1] *Department of Mathematics and Statistics, Texas Tech University, Lubbock, TX 79409-1042, USA.*
[2] *Laboratory of Montecuccolino, DIENCA, University of Bologna, Bologna, 40136, Italy.*
[3] *Department of Mathematical Sciences, George Mason University, Fairfax, VA 22030, USA.*

Abstract. In this paper, a multilevel domain decomposition approach based on multigrid methods for obtaining fast solutions for coupled engineering flow applications arising on complex domains is presented. The proposed technique not only allows solutions to be computed efficiently at the element level but also helps us to achieve proper accuracy, load balancing and computational efficiency. Numerical results presented demonstrate the robustness of the proposed technique.

AMS subject classifications: 65N30, 65N55, 65N12

Key words: Finite element methods, multigrid methods, domain decomposition.

1 Introduction

Over the last decade, there have been significant advances in developing solution methodologies for studying complex dynamics of coupled processes arising in a variety of applications that involve multiple interactions between flow, temperature and structures [3, 4, 9–11, 25, 33, 34, 37]. Domain decomposition techniques with non-matching grids have become increasingly popular in studying such coupled processes [2, 5, 29, 30]. In particular, they help achieve fast and accurate solutions to various applications involving coupled processes when used in conjunction with multigrid techniques [19,32]. They also allow coupling of different subdomains with nonmatching grids and different discretization techniques and the solution can be efficiently implemented even over parallel architectures.

---

*Corresponding author. *Email address:* `pseshaiy@gmu.edu` (P. Seshaiyer)

The purpose of this paper is to introduce a flexible domain decomposition approach that involves multigrid algorithm that will be used to study different engineering applications that involve flow mechanics. The first two applications involve flows through a channel with square cavities. The third and the fourth applications involve interaction between flow and large deforming structures.

2   Model and governing equations

We denote by $H^s(O), s \in \Re$, the standard Sobolev space of order s with respect to the set O, which is either the flow domain Ω, or its boundary Γ, or part of its boundary. Hence, we associate with $H^m(O)$, its natural norm $\|\cdot\|_{m,O}$. For $1 \le p < \infty$, the Sobolev space $W^{m,p}(O)$ is defined as the closure of $C^\infty(O)$ in the norm

$$\|f\|_{W^{m,p}(O)}^p = \sum_{|\alpha| \le m} \int_O \left| \left(\frac{\partial}{\partial x} \right)^\alpha f(x) \right|^p dx.$$

The closure of $C_0^\infty(O)$ under the norm $\|\cdot\|_{W^{m,p}(O)}$ will be denoted by $W_0^{m,p}(O)$. Whenever possible, we will neglect the domain label in the norm.

For vector-valued functions and spaces, we use boldface notation. For example, $\mathbf{H}^s(\Omega) = [H^s(\Omega)]^n$ denotes the space of $\Re^n$-valued functions such that each component belongs to $H^s(\Omega)$. Also we denote the space of square integrable functions having zero mean over Ω by $L_0^2(\Omega)$ and the space of solenoidal functions

$$\mathbf{V}(\Omega) = \{ \boldsymbol{u} \in \mathbf{H}^1(\Omega) \,|\, \nabla \cdot \boldsymbol{u} = 0 \}.$$

For $\Gamma_1 \subset \Gamma$ with non-zero measure, we also consider the subspace

$$\mathbf{H}^1_{\Gamma_1}(\Omega) = \{ \boldsymbol{v} \in \mathbf{H}^1(\Omega) \,|\, \boldsymbol{v} = \vec{0} \quad \text{on } \Gamma_1 \}.$$

Also, we denote $\mathbf{H}^1_0(\Omega) = \mathbf{H}^1_\Gamma(\Omega)$. For any $\boldsymbol{v} \in \mathbf{H}^1(\Omega)$, we write $\|\nabla \boldsymbol{v}\|$ for the semi-norm. Let $(\mathbf{H}^1_{\Gamma_1})^*$ denote the dual space of $\mathbf{H}^1_{\Gamma_1}$. Note that $(\mathbf{H}^1_{\Gamma_1})^*$ is a subspace of $\mathbf{H}^{-1}(\Omega)$, where the latter is the dual space of $\mathbf{H}^1_0(\Omega)$. The duality pairing between $\mathbf{H}^{-1}(\Omega)$ and $\mathbf{H}^1_0(\Omega)$ is denoted by $< \cdot, \cdot >$.

Let $\boldsymbol{g}$ be an element of $\mathbf{H}^{1/2}(\Gamma)$. It is well known that $\mathbf{H}^{1/2}(\Gamma)$ is a Hilbert space with norm

$$\|\boldsymbol{g}\|_{\frac{1}{2},\Gamma} = \inf_{\boldsymbol{v} \in \mathbf{H}^1(\Omega); \gamma_\Gamma \boldsymbol{v} = \boldsymbol{g}} \|\boldsymbol{v}\|_1,$$

where γ_Γ denotes the trace mapping $\gamma_\Gamma : \mathbf{H}^1(\Omega) \to \mathbf{H}^{1/2}(\Gamma)$. We let $(\mathbf{H}^{1/2}(\Gamma))^*$ denote the dual space of $\mathbf{H}^{1/2}(\Gamma)$ and $< \cdot, \cdot >_\Gamma$ denote the duality pairing between $(\mathbf{H}^{1/2}(\Gamma))^*$ and $\mathbf{H}^{1/2}(\Gamma)$.

2.1 Model problem and variational formulation

Let us consider the time-dependent Navier-Stokes problem describing the flow of a fluid in a region $\Omega \in \Re^2$ given by:

$$\rho \frac{\partial u}{\partial t} - \mu \Delta u + (u \cdot \nabla)u + \nabla p = f \quad \text{in } \Omega \times (0,T), \tag{2.1}$$

$$\nabla \cdot u = 0 \quad \text{in } \Omega \times (0,T), \tag{2.2}$$

$$u = g \quad \text{on } \Gamma_1 = \partial\Omega \times (0,T), \tag{2.3}$$

where ρ and μ are the density and the viscosity, f is the body force and g is the prescribed imposed velocity over Γ_1 satisfying the compatibility condition.

Let $f \in \mathbf{H}^{-1}(\Omega)$ and $g \in \mathbf{H}^{1/2}(\Gamma_1)$. Then the velocity, the pressure and the stress vector fields $(u,p,\tau) \in \mathbf{H}^1(\Omega) \times L^2(\Omega) \times \mathbf{H}^{-1/2}(\Gamma)$ satisfy the weak variational form of the unsteady incompressible Navier-Stokes equations given by

$$<\rho \frac{\partial u}{\partial t}, v> + a(u,v) + c(u;u,v) + b(v,p) + <\tau, v>_\Gamma = <f,v>, \tag{2.4}$$

$$b(u,r) = 0, \tag{2.5}$$

$$<u,s>_{\Gamma_1} = <g,s>_{\Gamma_1} \tag{2.6}$$

for all $(v,r,s) \in \mathbf{H}^1(\Omega) \times L^2(\Omega) \times \mathbf{H}^{-1/2}(\Gamma_1)$. Here the continuous bilinear forms are defined as

$$a(u,v) = 2\mu \int_\Omega D(u):D(v)dx \qquad \forall u,v \in \mathbf{H}^1(\Omega), \tag{2.7}$$

$$b(v,r) = -\int_\Omega r\nabla \cdot v dx \qquad \forall r \in L^2(\Omega), \forall v \in \mathbf{H}^1(\Omega), \tag{2.8}$$

and the trilinear form

$$c(w;u,v) = \rho \int_\Omega (w \cdot \nabla)u \cdot v dx = \sum_{i,j=1}^{2} \rho \int_\Omega w_j \left(\frac{\partial u_i}{\partial x_j} \right) v_i dx \quad \forall w,u,v \in \mathbf{H}^1(\Omega). \tag{2.9}$$

For details concerning the function spaces, the bilinear and the trilinear forms and their properties, one may consult [18, 35]. In system (2.4)-(2.6),

$$\tau = -\mu \nabla u \cdot n + p n \in \mathbf{H}^{-1/2}(\Gamma)$$

is the stress vector. In domain decomposition methods, its computation across different subdomains is an important issue. The interested reader can consult [18] and citations therein. Existence and uniqueness results for solutions of the above system are well known; see, e.g., [15–17].

2.2 Non-conforming domain decomposition

Let the fluid domain Ω be partitioned into m non-overlapping sub-domains $\{\Omega^i\}_{i=1}^m$ such that the closure of the union of Ω_i is equivalent to the closure of Ω. Note that the presentation in the paper is in two dimensions and one can extend this to three dimensions which will be considered in a forthcoming paper. Hence we consider $\partial\Omega^i \cap \partial\Omega^j$ ($i \neq j$) to be either empty, a vertex, or a collection of edges of Ω^i and Ω^j. In the latter case, we denote this interface by Γ^{ij} which consists of individual common edges from Ω^i and Ω^j. The velocity, the pressure and the stress field $(u^i, p^i, \tau^{ij}) \in \mathbf{H}^1(\Omega^i) \times L^2(\Omega^i) \times \mathbf{H}^{-1/2}(\Gamma^{ij}))$ satisfy

$$<\rho\frac{\partial u^i}{\partial t}, v^i> + a(u^i, v^i) + c(u^i; u^i, v^i) + b(v^i, p^i) + <\tau^{ij}, v^i>_{\Gamma^{ij}} = <f, v^i>, \tag{2.10}$$

$$b(u^i, r^i) = 0, \tag{2.11}$$

$$<u^i, s^i>_{\Gamma_1^i} = <g, s^i>_{\Gamma_1^i}, \tag{2.12}$$

$$<u^i - u^j, s^{ij}>_{\Gamma^{ij}} = 0 \tag{2.13}$$

for all $v^i \in \mathbf{H}^1(\Omega^i)$, $r^i \in L^2(\Omega_i)$, $s^i \in \mathbf{H}^{-1/2}(\Gamma_1^i)$ and $s^{ij} \in \mathbf{H}^{-1/2}(\Gamma^{ij})$, for $i = 1, 2, \cdots, m$. Here Γ_1^i is $\Gamma \cap \bar{\Omega}_i$ and the stress on the main boundary Γ is set to be equal to zero where Dirichlet boundary conditions are not imposed. Note that in the continuous case, on the boundary Γ^{ij}, the velocity vectors, u^i and u^j, and the stress vectors τ^{ij} and τ^{ji} are in the same spaces, $\mathbf{H}^{1/2}(\Gamma^{ij})$ and $\mathbf{H}^{-1/2}(\Gamma^{ij})$ respectively, namely

$$u^i = u^j \quad \text{and} \quad \tau^{ij} = -\tau^{ji},$$

where the equivalences are in the strong form. Also we remark that the computation of $\tau^{ij} \in \mathbf{H}^{-1/2}(\Gamma^{ij})$ cannot be in general accurate, especially at corners or singular points, due to its poor regularity. However it is possible to compute τ^{ij} from u^i by using the concept of extended function and extended domain. The reader interested in the numerical computation of the stress vector can refer to [14]. In order to facilitate the computation of the stress at the boundary or mesh interfaces we introduce the extended domain $\hat{\Omega}^i$ of Ω^i as $\Omega = \hat{\Omega}^i$. The solution u^i over the domain Ω^i can be extended by using the standard theory [17]. In the rest of the paper we write u^i to denote the function over Ω^i and $\hat{u}^i$ its extension to Ω. The stress τ^{ij} can then be computed via,

$$<\tau^{ij}, \hat{v}^i>_{\Gamma^{ij}} = - <\frac{\partial \hat{u}^i}{\partial t}, \hat{v}^i> - a(\hat{u}^i, \hat{v}^i) - c(\hat{u}^i; \hat{u}^i, \hat{v}^i) - b(\hat{v}^i, \hat{p}^i) + <f, \hat{v}^i> \tag{2.14}$$

for all $\hat{v}^i \in \mathbf{H}^1_{\Gamma_1}(\Omega - \Omega^i)$ which also yields an expression for computing the lagrange multipliers τ^{ij}.

3   Finite element discretization

3.1   The multilevel domain decomposition

Let us introduce a finite element discretization in each subdomain Ω^i through the mesh parameter h which tends to zero. We consider our discretized domain Ω_h to be partitioned into m non-overlapping polygonal subdomains Ω_h^i. Now, by starting at the multi-grid coarse level l_0, we subdivide Ω_h^i and consequently Ω_h into triangles or rectangles by unstructured families of meshes T_h^{i,l_0}. At this coarse level l_0, as at the generic multigrid level l, the triangulation over all Ω_h^i are dependent and satisfy finite element compatibility constraints along the interfaces Γ_h^{ij}. Based on the simple element midpoint refinement, different multigrid levels can be built to reach a complete unstructured mesh $T_h^{i,l}$ of finite elements over the entire domain Ω_h at the top finest multigrid level n_t. Let the maximum size of the triangulation of the multigrid level l be h_l. For details on multigrid levels and their construction one may consult [6,27,36]. Now we have complete unstructured meshes at each multigrid level in a standard finite element fashion with compatibility enforced across all the element interfaces built over midpoints refinements. Over every macro domain Ω_h^i the Navier-Stokes equation can be solved over a different level l_i generating a solution mesh over Ω_h consisting of different meshes over each subdomain. Let us denote $\Omega_{h_{l_i}}^i$ to be the subdomain i where the solution will be computed at the finest multigrid level l_i, with h_{l_i} denoting the maximum size of the triangulation of subdomain. It should be noted that the multigrid levels at which the solution is computed over individual subdomains Ω_h^i and Ω_h^j maybe different from each other, with no compatibility enforced across the interface Γ_h^{ij}.

The recursive generation of finer grid levels may be used to generate an appropriate mesh discretization in the boundary layers subdomains, where generally a finer mesh is needed. This can be achieved with a correct/smart choice of the coarse level triangulation and eventually with midpoint refinement made only in preferential direction: perpendicular to the boundary.

Finite element approximation spaces can be generated regularly, as function of the characteristics length h_l over each multigrid level l resulting in different approximation spaces over the solution mesh Ω_h^i. Note that on the solution mesh, we compute the velocity field u_h^i at the level l over $\Omega_{h_l}^i$ but, the extended function $\widehat{u}_h^i$ is defined over all Ω_h. There maybe parts of the domain where the solution is not computed at the top level but a projection operator from the coarser level can always be used to approximate the solution over the extended domain Ω_h and therefore an approximation to the extended function $\widehat{u}_h^i$ is always available. This extended function has the same value at those nodes in the coarser mesh that are included in the finest mesh. This is always the case if the different levels are generated by successive midpoint refinements.

Let us choose the families of finite-dimensional spaces $\mathbf{X}_{h_l} \subset \mathbf{H}^1(\Omega)$ and $S_{h_l} \subset L_0^2(\Omega)$. We make the following assumptions on $\mathbf{X}_{h_l}$ and S_{h_l} for the extended functions defined

over Ω_h (see, e.g., [16]):

(a) *Approximation hypotheses:* For each multigrid level l there exists an integer l_1 and a constant C, independent of $h_l, \widehat{u}$ and p, such that

$$\inf_{\widehat{u}_{h_l} \in \mathbf{X}_{h_l}} \|\boldsymbol{u} - \widehat{u}_{h_l}\|_1 \leq Ch_l^k \|\boldsymbol{u}\|_{k+1} \quad \forall \boldsymbol{u} \in \mathbf{H}^{k+1}(\Omega) \cap \mathbf{H}_0^1(\Omega), \ 1 \leq k \leq l_1,$$

$$\inf_{\widehat{p}_{h_l} \in S_{h_l}} \|p - \widehat{p}_{h_l}\| \leq Ch_l^k \|p\|_k \quad \forall p \in H^k(\Omega) \cap L_0^2(\Omega), \ 1 \leq k \leq l_1;$$

(b) *Inf-sup or LBB condition:* There exists a constant C', independent of h_l, such that

$$\inf_{0 \neq \widehat{q}_{h_l} \in S_{h_l}} \sup_{0 \neq \widehat{u}_{h_l} \in \mathbf{X}_{h_l}} \frac{\int_\Omega \widehat{q}_{h_l} \nabla \cdot \widehat{u}_{h_l} \, d\boldsymbol{x}}{\|\widehat{u}_{h_l}\|_1 \|\widehat{q}_{h_l}\|_0} \geq C' > 0$$

for all multigrid levels $l \leq n_t$. This condition assures the stability of the Navier-Stokes discrete solutions.

(c) Let $\mathbf{P}_{h_l} = X_{h_l}|_{\partial\Omega}$, i.e., $\mathbf{P}_{h_l}$ consists of all the restrictions of functions belonging to X_{h_l} to the boundary Γ. For the subspaces $\mathbf{P}_{h_l} = X_{h_l}|_\Gamma$, we assume the approximation property: For each multigrid level l there exists an integer l_1 and a constant C, independent of $\boldsymbol{s}$ such that

$$\inf_{0 \neq \boldsymbol{s}_{h_l} \in \mathbf{P}_{h_l}} \|\boldsymbol{s} - \boldsymbol{s}_{h_l}\|_{-\frac{1}{2}, \Gamma} \leq Ch_l^k \|\boldsymbol{s}\|_{k-\frac{1}{2}} \quad \forall \boldsymbol{s} \in H^{k-\frac{1}{2}}(\Gamma), \ 1 \leq k \leq l_1.$$

See [14, 16] for details concerning the approximation on the boundary. With these hypotheses we can build regular conforming approximations over each grid while the approximate solution belongs to $\mathbf{X}_{h_l}$ corresponding to the subdomain $\Omega^i_{h_l}$.

The multilevel domain decomposition problem over the domains Ω^i_h $(i = 1, 2, \cdots, m)$ solved on the level l_i surrounded by the domains Ω^j_h with $j \in I_i$ (I_i being the set of the neighboring regions of i) can be obtained by discretizing (2.10)-(2.13). Given $f \in \mathbf{L}^2(\Omega)$ and $g \in \mathbf{H}^{1/2}(\Gamma)$, employing an implicit Euler time discretization with time step Δt, our problem then becomes the following:

Find $(\boldsymbol{u}^i_{h_{l_i}, n}, p^i_{h_{l_i}, n}, \tau^{ij}_h) \in \mathbf{X}_{h_{l_i}}(\Omega^i_h) \times S_{h_{l_i}}(\Omega^i_h) \times \mathbf{P}_{h_{l_i}}(\Gamma^{ij}_h)$ satisfying the weak form of the Navier-Stokes equations

$$\frac{1}{\Delta t} < \boldsymbol{u}^i_{h_{l_i}, n}, \boldsymbol{v}^i_{h_{l_i}} > + a(\boldsymbol{u}^i_{h_{l_i}, n}, \boldsymbol{v}^i_{h_{l_i}}) + c(\boldsymbol{u}^i_{h_{l_i}, n}; \boldsymbol{u}^i_{h_{l_i}, n}, \boldsymbol{v}^i_{h_{l_i}}) + b(\boldsymbol{v}^i_{h_{l_i}}, p^i_{h_{l_i}, n})$$

$$+ < \tau^{ij}_{h, n}, \boldsymbol{v}^i_{h_{l_i}} >_{\Gamma^{ij}_h} = \frac{1}{\Delta t} < \boldsymbol{u}^i_{h_{l_i}, n-1}, \boldsymbol{v}^i_{h_{l_i}} > + < \boldsymbol{f}, \boldsymbol{v}^i_{h_{l_i}} >, \tag{3.1}$$

$$b(\boldsymbol{u}^i_{h_{l_i}, n}, r^i_{h_{l_i}}) = 0, \tag{3.2}$$

$$< \boldsymbol{u}^i_{h_{l_i}, n}, \boldsymbol{s}^i_{h_{l_i}} >_{\Gamma_{1h}} = < \boldsymbol{g}^i_{h_{l_i}}, \boldsymbol{s}^i_{h_{l_i}} >_{\Gamma_{1h}}, \tag{3.3}$$

$$< P_{l_i, l_k}(\boldsymbol{u}^i_{h_{l_i}}) - P_{l_j, l_k}(\boldsymbol{u}^j_{h_{l_i}}), \boldsymbol{s}^{ij}_{h_{l_k}} >_{\Gamma^{ij}_h} = 0, \tag{3.4}$$

$$\forall \boldsymbol{v}^i_{h_{l_i}} \in \mathbf{X}_{h_{l_i}}(\Omega^i_h) \cap \mathbf{H}^1_{\Gamma_1}(\Omega^i_h), \quad \forall r^i_{h_{l_i}} \in S_h(\Omega^i_h), \quad \forall \boldsymbol{s}^i_{h_{l_i}} \in \mathbf{P}_{h_{l_k}}(\Gamma^i_{1h}),$$

$$\forall \boldsymbol{s}^{ij}_{h_{l_k}} \in \mathbf{P}_{h_{l_k}}(\Gamma^{ij}_h) \quad \text{for} \ \ n=1,2,\cdots,N \ \ \text{and} \ \ i=1,2,\cdots,m,$$

where $j \in I_i$, $\Gamma^i_{1h} = \Gamma_{1h} \cap \partial\Omega^i_h$ and $l_k = \max\{l_i, l_j\}$ over the multigrid levels available at the boundary Γ^{ij}_h. Here $P_{l_i, l_k}(\boldsymbol{u})$ are canonical prolongation operators and in order to ensure maximum accuracy they project the velocity from the level l_i to the level l_k which is the finest grid present on the boundary Γ^{ij}_h. For details and properties of these operators, one can consult [6,21] and citations therein. With this hypotheses, the lagrange multipliers $\boldsymbol{\tau}^{ij}_h$ can also be discretized and projected on the finest grid available on Γ^{ij}_h. Since the mesh on the multigrid are unstructured and quite openly constructed the mesh between the subdomain Ω^i_h and the neighboring subdomain Ω^i_h can be quite different, as mentioned earlier. Moreover, very fine meshes in the region of interest and coarse meshes elsewhere can be handled with little effort.

Equation system (3.1)-(3.4) is non-linear due to the term $c(\boldsymbol{u}^i_{h_{l_i},n}; \boldsymbol{u}^i_{h_{l_i},n}, \boldsymbol{v}^i_{h_{l_i}})$. For its treatment, we have adopted the FEM flux-corrected transport algorithm proposed in [40], where the non-linear operator is re-written in term of fluxes and linearized. By using this technique, as soon as a new value of velocity is available, it is possible to update the linearized convective term $c(\boldsymbol{a}; \boldsymbol{u}^i_{h_{l_i},n}, \boldsymbol{v}^i_{h_{l_i}})$ with no additional assembly time. In all numerical examples analyzed in this work the Reynolds number is always laminar and no-flux corrections are used.

3.2 Solution methodology

We solve the system (3.1)-(3.4) by computing simultaneously the solution for both pressure and velocity. In order to optimally solve this system involving the unknown variable $\boldsymbol{\tau}^{ij}_h$, we choose a Vanka smoother [22–24, 26, 27, 36, 38] which involves the solution of the minimal number of degrees of freedom for standard conforming Taylor-Hood finite elements but meets enough requirements of robustness. This smoother can be considered as block Gauss-Seidel method, where one block consists of a small number of degrees of freedom. A typical smoothing step consists of a loop over all the blocks, solving only the equations involving the unknowns inside the elements that are around the considered pressure vertices. The velocity and pressure variables are updated many times in one smoothing step. The Vanka smoother, employed herein involves the solution of a small number of degrees of freedom given by the conforming Taylor-Hood finite element discretization used. For this kind of element the pressure is computed in the vertices while the velocity field is computed in both the vertices and the midpoints. Over the internal part of the generic subregion Ω^i_h, where there are no boundary elements, our Vanka-block consists of an element and all its neighboring elements. We solve for all the degrees of freedom inside the block, with boundary condition taken on the external boundaries. For example, in Fig. 1, our block consists of four vertex points and 12 midpoints to be
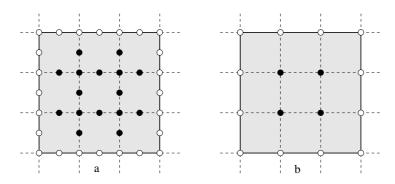
Figure 1: Unknowns (black circles) and boundary conditions (white circles) shown for (a) the velocity field u_h (b) pressure p_h for our Vanka-block smoother.

solved, for a total of 36 unknowns. We have also used different blocks with different performances but we have found this particular block to be very robust and reliable even at high Reynolds numbers. Examples of computations with this kind of solvers can be found in [27, 36].

It should be noticed that if no boundaries Γ_h^{ij} cut the computational block, no Lagrange multiplier terms $<\tau_h^{ij}, v_{h_{l_i}}^i>_{\Gamma_h^{ij}}$ should be considered. In the other case the boundary Γ_h^{ij} will become the boundary of the computational block as well. Two different subcases are possible: (a) the block belongs to the subdomain with the finest mesh; (b) the block belongs to the subdomain with the coarsest mesh. In case (a) the velocity and the pressure on the boundary are considered as given boundary conditions from the coarsest mesh, after projection, and no stress tensor τ_h^{ij} should be considered. In case (b) the velocity and the pressure are computed on the boundary, while each Lagrange multiplier term $<\tau_h^{ij}, v_{h_{l_i}}^i>_{\Gamma_h^{ij}}$ is given explicitly as a linear combination (restriction) of the corresponding Lagrange multiplier terms on the fine grid. It should be noticed that on the fine grid the Lagrange multiplier terms are evaluated using (2.14); in other words the computational block can be considered as an extended computational block, part in the coarse subdomain and part in the fine subdomain with no boundary Γ_h^{ij}. This corresponds to an overlapping domain decomposition strategy.

To increase the convergence rate, the Vanka-smoother is coupled with a standard V-cycle multigrid algorithm. The multigrid does not change the nature of the solver, but allows the information to travel faster between different parts of the domain. A global rough solution is evaluated in the coarsest mesh and propagated immediately all over the domain. Solving the equation system in finer and finer meshes improves the solution details, but at the same time reduces the propagation of the information inside the domain. However this does not affect the global convergence rate, since the influence of small local changes is more and more irrelevant as soon as the distance increases. The analysis of the convergence of Vanka-type multigrid solvers for Navier-Stokes can be found in [26]. In order to prove the convergence of the proposed multilevel domain decompo-

sition algorithm, we plan to combine the approach used in [26] together with Schwarz alternating type approaches. We are currently working on this proof and it will be the focus of a forthcoming paper. At this moment, we have proved geometrical convergence only for elliptic problems.

4   Numerical experiments

In this section, we apply the flexible domain decomposition approach introduced in this paper to study different engineering applications that involve flow mechanics. The first two application involve flows through a channel with a square cavities. The third application involves a flow-structure interaction that describes a biological application that involves blood flow interacting with a deforming aneurysm. In the fourth application a fluid-structure benchmark problem recently proposed [3], that involves large deformation of a thin membrane structure is considered.

4.1   Flow through a channel with one square cavity

The first numerical experiment is to investigate the effectiveness of the domain decomposition approach described to study flow through a channel with a square cavity. The Reynolds number for the experiment is set to be 250. We assume that the fluid flows in a symmetric channel between two parallel plates. In the channel interior there are two symmetric square cavities and due to the symmetry only half of the domain is used and the simulation is modeled as in Fig. 2 computing only the flow close to the cavity.
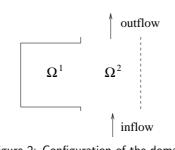

Figure 2: Configuration of the domain.

The computational domain Ω_h is a rectangular region divided in two subregions: the cavity Ω_h^1 and the channel Ω_h^2. The flow enters from the bottom of the subregion Ω_h^2 and reaches the outlet at the top of Ω_h^2. Therefore we impose a symmetric parabolic flow profile at the inlet with unit maximum velocity on the symmetric line and outflow boundary condition at the top of the subregion Ω_h^2. On the right side of Ω_h^2 we impose symmetric boundary conditions. On the cavity Ω_h^1 homogeneous Dirichlet boundary conditions are enforced over the three sides of the subregion Ω_h^1. The fluid enters into the cavity from the right side of Ω^1 domain and generates a vortex in the cavity. Since the flow is laminar inside the channel Ω_h^2 we keep the finest grid on the domain Ω_h^1 and try
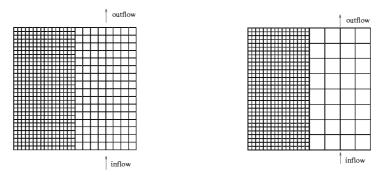
Figure 3: Computational domain showing coupled multigrid levels $l_4 - l_3$ (on the right) and level $l_4 - l_2$ (on the left).

to use a coarse grid on the channel region Ω^2. We consider an unstructured coarse mesh of isoparametric rectangular finite elements for P_2/P_1 velocity/pressure representation. After the construction of the mesh at the level l_0 the other mesh levels l_i ($i = 1,2,3,4$) are generated by an unstructured grid generator by midpoint refinements.

Fig. 3 (on the right) shows the grid configuration for the domain decomposition when the mesh level l_4 in Ω_h^1 is coupled with the level l_3 and (on the left) with level l_2 in Ω_h^2. In this test we try to compute the solution in domain decompositions with three different mesh configurations: A) the standard configuration where the solution is computed over Ω_h at level l_4; B) the mesh configuration where the solution is computed at mesh level l_4 (over Ω_h^1) and level l_3 (over Ω_h^2) ; C) the mesh configuration where the solution is computed at l_4 (over Ω_h^1) and level l_2 (over Ω_h^2). In the configuration A of this experiment the solution is obtained at the level l_4 by a standard multigrid technique relaxing, projecting and interpolating over all the available levels (from l_0 to l_4) and it is stopped when the residual of the linear system is 10^{-4} for the velocity with referee velocity of $1m/s$. In the case B and C the multigrid V cycle is regularly applied over the coarse grid at the level l_3 and l_2 respectively.
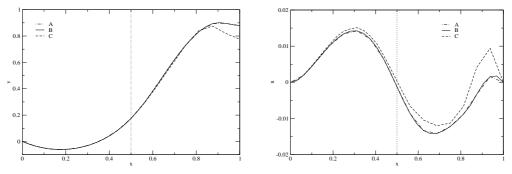

Figure 4: The v and u velocity components at the centerline as a function of x.

In Figs. 4-5 the extended velocity $\widehat{u}_{h_{l_4}} = (u,v)$ is plotted for the different mesh configuration A, B and C The extended solution for case A is the regular solution $u_{h_{l_4}}$ defined
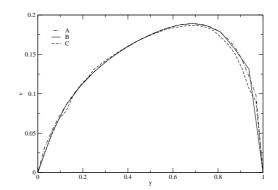
Figure 5: The v component of the velocity field along the mesh interface Γ_h^{12}.

over the domain Ω_h. In the cases B and C the velocity field is computed at mesh level l_3 and l_1 respectively and projected but not solved over the mesh on the level l_4. The results in Fig. 4 are satisfactory and the difference between the solution in A and the solution in the configuration C is not due to the use of different meshes but to the fact that the grid at the level l_2 cannot handle the sharp velocity gradients. Nevertheless, the results show that one can efficiently use domain decomposition with different meshes to capture important features of the flow. By refining only in the regions of interest, one can still obtain a good solution at the cost of lower number of degrees of freedom.

4.2 Flow through a channel with eight square cavities

In the second numerical experiment we illustrate an example in which the multilevel method can be efficiently applied to problems in fluid dynamics. We consider challenging domains where small regions of fluids are coupled with large ones, for example the geometry in Fig. 6 where a L-shape domain Ω_0 is shown with eight unitary small square cavities Ω_i $i = 1, \cdots, 8$. Here the use of a single grid level leads to a very cumberstone implementation since the cavity flow must be solved with different resolution. As in the previous test the first multigrid level l_0 is the coarse mesh designed to contain all the relevant information such as boundary conditions and geometric details. The boundary conditions for this problem are inflow boundary conditions on the bottom of the first branch with parabolic profile (max vel. $1m/s$) and outflow boundary conditions on Γ_2. Dirichlet boundary conditions are applied in the rest of the boundary. The computations are performed in laminar regime for Reynolds number of 20 and rectangular finite elements Q_2/Q_1 velocity/pressure are used. The other levels l_i ($i=1,2,3,4$) are generated by midpoint refinement. The computations in the cavity regions Ω_i ($i=1,2,3,\cdots,8$) should be accurate and therefore solved on the finest grid l_4. The levels l_4, l_3, l_2 or l_1 are considered for computation over Ω_0. In Figs. 6-7 we can see the multilevel configurations on nonmatching grids considered in this test when the mesh level l_4 over the cavities Ω_i is coupled with the mesh levels l_3, l_2 and l_1 over Ω_0 (case B, C and D respectively). The so-
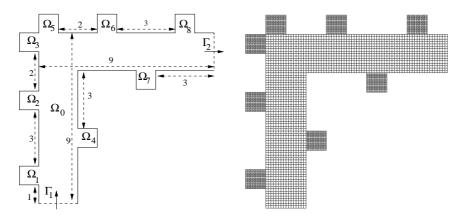
Figure 6: Geometry for the numerical experiment 2 on the left and domain decomposition with coupled levels l_4-l_3 (case B) on the right.
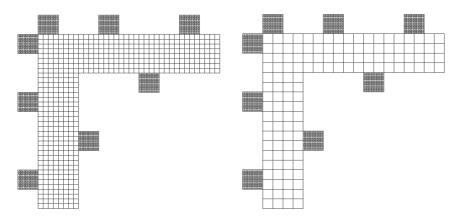

Figure 7: Multilevel decomposition with coupled levels l_4-l_2 (case C) on the left and with coupled levels l_4-l_1 (case D) on the right.

lution, over the uniform level l_4 (case A), is taken as reference solution and is obtained by standard V-cycle multigrid with residual norm in velocity and pressure approximately 10^{-13}. The reference velocity is $1m/s$ which is the maximum velocity of the parabolic inflow profile at the inlet. The procedure computes the Lagrange multipliers τ_h^{ij} on the boundary, implicitly. In this case the solution $\mathbf{u}_{h_{l_i}}^i$ is projected by the standard finite element projection operator (the same of the standard multigrid) over the finest grid at level l_4 obtaining the extended solution for $\widehat{u}_h$ over Ω_0. The extended solution generates the boundary conditions for the computation of the solution on the finest grid, which is the union of all Ω_i ($i=1,2,\cdots,8$).

The solution along the channel centerlines is reproduced accurately in both branches for all cases A, B, C and D. The solution over all the regions Ω_i for $i=1,2,\cdots,8$ cannot be captured with a low resolution mesh (for example level l_2) and therefore the multilevel technique becomes a powerful tool in such configurations. Even with very coarse mesh in

the channel the fine grid on the cavity allows a good and accurate simulation of the cavity flows. As example in Fig. 8 the *v*-component of the velocity field is plotted as across the cavities in the regions Ω_1, Ω_2 as a function of the *x*-coordinate and Ω_6, Ω_7 as a function of the *y*-coordinate from the top to the bottom and from left to right. The velocity field computations over the different configurations *A*, *B* and *C* cannot be distinguished. The solution for the case *D* shows that the solution is starting to be different due to the very coarse mesh matching.
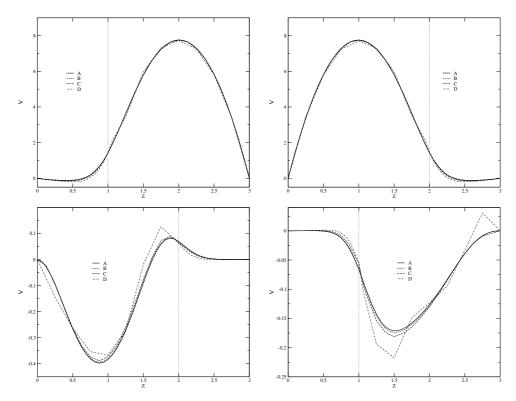

Figure 8: V-component along the midline in the cavity regions Ω_1 (top left), Ω_2 (top right) as a function of the x-coordinate and Ω_6 (bottom left) Ω_7 (bottom right) as a function of the y-coordinate for the different case *A*,*B*,*C* and *D*.

By using nonmatching grids, the number of nodes (and hence the degrees of freedom) decreases and so does the necessary cpu time. In Table 1 a quantitative comparison between the number of unknowns and the relative CPU time is shown. There is clear advantage of using domain configuration *B* with respect to *A* and of using domain configuration *C* with respect to *A* and *B*. From a computational point of view case *D* is not much better then case *C*. There is a saturation due to the fact that in both cases most of the computational time is spent in the cavity regions where the fine level l_4 is used. Furthermore we have already pointed out that in case *D* the solution slightly degenerates. This result suggests that the better configuration is not necessarily the one with the lowest number of nodes.

Table 1: Results for the computational experiment 2.

case	grids	unknowns	rel. cpu time
A	$l_4 - l_4$	53504	1
B	$l_4 - l_3$	22210	0.425
C	$l_4 - l_2$	14124	0.275
D	$l_4 - l_1$	11962	0.243

4.3 Bifurcating artery with aneurysm

In this section, the performances of the computational methodology developed in this paper are tested for a specific biological application that involves a coupled flow-structure interaction problem. In this last decade there has been a lot of interest in developing mathematical models to understand the vasculature better [7,8,28]. More specifically, we model the effects on the morphology of an aneurysm due to changes in the blood pressure in a hemodynamics problem. The motivation for considering this application is because cardiovascular diseases and cerebral disorders, such as arteriosclerosis or cerebral aneurysm, are reported to depend on hemodynamics factors. It is therefore important to obtain detailed information on the hemodynamics and structural quantities of the cardio and cerebral vascular systems.

According to medical statistics [39] and clinical observations, pathological alterations such as cerebral aneurysm occur mainly in region of arterial branching where the aneurysm tends to appear and to grow at the apex of artery bifurcations. A quite complex flow structure interaction is associated with the biological problem. In Fig. 9 the flow computational domain Ω is shown together with all the geometrical details. It is possible to recognize the inlet region Γ_1 and the two outlet regions Γ_2 and Γ_3, on the top and bottom branches. The circular cavity region on the apex of the bifurcation is the aneurysm which deforms preserving its circular shape. The flow computational domain Ω is divided into the two subdomains Ω^1 and Ω^2, where Ω^1 is the left part of the main channel and Ω^2 is the other part, consisting of the ending right part of the main channel, the top and the bottom branches, and the aneurysmal cavity.

We assume that the boundary of the domain Ω consists of a rigid and a deformable part. The deformable part models the aneurysm, which is the common boundary Γ_{SF} where the fluid-structure interaction occurs (where the subscripts F and S stand for fluid and solid respectively.) In Fig. 9, Γ_{SF} is the arc BC with initial radius of R_0. Let λ be the stretch ratio between the deformed radius r and the initial undeformed radius R_0. We compute the two-dimensional solution of the coupled problem assuming that the arc BC deforms according to the relation

$$P(r) = P_0 + \frac{C}{r}\left(1 - \frac{1}{\lambda^6}\right), \tag{4.1}$$

where P is the average pressure in the aneurysmal cavity and C is a constant equal to

$0.88N/m$. Here we have assumed that the aneurysm deforms always preserving its circular shape and remains tangent to the two branches.
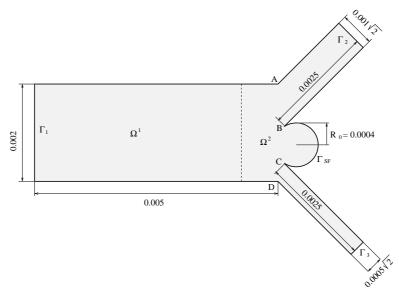

Figure 9: Bifurcating artery with an aneurysm.

In Fig. 10, the radius-pressure relation is shown around the chosen equilibrium point (P_0, R_0). This relation is derived by assuming a neo-Hookean material law for the membrane [1]. Note that this model has been chosen only for the purposes of illustrations; others constitutive relations for soft tissues [12, 20, 31] may also be employed.

To simulate the flow-structure interaction, the flow described by Eqs. (2.10)-(2.13) is coupled with a structural model through a governing equation given in operator form

$$\mathcal{A}(\boldsymbol{u}, p) = F(\boldsymbol{x}_S), \tag{4.2}$$

where the right hand side may be a non-linear function that depends on the displacement of the structure. The conditions of displacement compatibility, $\boldsymbol{x}_F = \boldsymbol{x}_S$, and force equilibrium, $\boldsymbol{f}_F = \boldsymbol{f}_S$, along the structure-fluid interfaces Γ_{SF} are satisfied. The fluid is fully coupled to the structure that can undergo nonlinear response due to large deformations or inelasticity. The fluid and solid equations are solved iteratively, in succession, always using the latest information provided by the other part of the coupled system. From the solution of the fluid-dynamics problem the pressure and the velocity field are evaluated, and the boundary forces for the structural problem are computed. The structural dynamics system is then solved for the displacements, and modification of the fluid domain Ω, satisfying the displacement compatibility conditions, $\boldsymbol{x}_F = \boldsymbol{x}_S$, are made along the common boundaries Γ_{SF}. The whole procedure is repeated iteratively until convergence for both the fluid and the structural parts is reached.
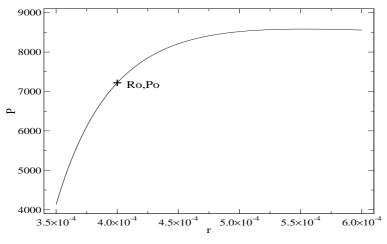
Figure 10: Radius-pressure constitutive relation.

The first multigrid level $l=0$ is the coarse mesh designed to contain all relevant information such as boundary conditions and geometric details. The mesh is an unstructured coarse mesh of isoparametric rectangular finite elements Q_2/P_1 for the velocity/pressure representation. The other levels ($l=1,2,3$) are generated by midpoint refinement techniques. The computations in the outlet region Ω_h^2 should be accurate and therefore solved on the finest grid, $l=3$. The mesh levels $l=3,2$ and 1 are considered for computations over the region Ω_h^1. Fig. 11 on the top, shows the grid configuration for the mesh levels $l=3$ (top left) and $l=2$ (top right). Fig. 11 on the bottom, shows two non-conforming grid configurations. On the bottom left, the subdomains Ω_h^1 and Ω_h^2 are considered at the two different levels $l=1$ and $l=3$. On the bottom right the same subdomains are considered at the two different levels $l=2$ and $l=3$.

First we compute the solution of our coupled problem for the stationary equations by using the multilevel configuration l_3-l_2 previously described. The parallelization of this problem over a multiple processor architecture computer is done by simply clustering blocks of elements. There are numerous possibilities for this but if the clustering is performed at the level l_0 then this does not introduce any supplementary work since it is strictly embedded in the multigrid technique.

We set $\rho=1060kg/m^3$, $\mu=0.25Kg/ms$ and initial radius $R_0=4.00\times10^{-4}m$. The initial pressure evaluated at $R_0=4.00\times10^{-4}m$ with velocity $u=0.3m/s$ is $P_0=7220Pa$ as shown in Fig. 10. For an initial steady velocity of $u=3.55\times10^{-1}m/s$ applied, the system increases the pressure in the region of interest to $8517Pa$ with corresponding deformation of the radius to $4.99\times10^{-4}m$. The initial and final deformed mesh is shown in Fig. 12.

Next we perform the simulation for the time dependent case. Again we assume the configuration in Fig. 11 with $\rho=1060kg/m^3$, $\mu=0.25Kg/ms$ with a time dependent inlet velocity $u=0.3+0.058\sin(t)m/s$. The initial radius is $R_0=4.00\times10^{-4}m$ with $u=0.3m/s$ and $P_0=7220Pa$. The deformed body is subject to the law in (4.1) and the radius oscillates and the deformed body expands and contracts periodically accordingly.
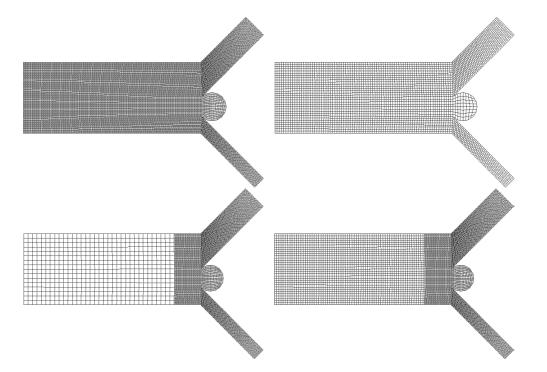
Figure 11: Grid configurations at the mesh levels $l=3$ and $l=2$, on the top, and non-conforming grid configurations $\Omega_h^{1,1} - \Omega_h^{2,3}$ and $\Omega_h^{1,2} - \Omega_h^{2,3}$, on the bottom.
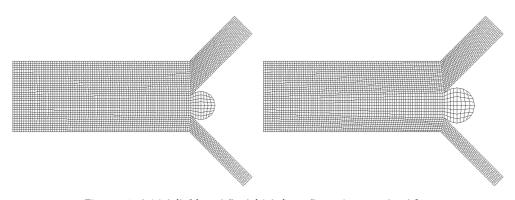

Figure 12: Initial (left) and final (right) configuration over level l_2.

For the simulation, maximum and minimum radii are obtained as $R_{max} = 5.264 \times 10^{-4} m$ $(R_{max}/R_0 = 1.316)$ and $R_{min} = 3.701 \times 10^{-4} m (R_{min}/R_0 = 9.254 \times 10^{-1})$, respectively, at $P_{max} = 8571 Pa$ and $P_{min} = 5814 Pa$. The pressure-velocity oscillations are compared when the body in Ω_h^4 is considered rigid (case 1) and deformed (case2). Figs. 13-14 show a comparison when the deformed body is allowed to oscillate and when it is kept fixed. In Fig. 13 we plot the u-component (left) and the v-component (right) of the velocity field along the line $ABCD$ as defined in Fig. 11 at time $t = \pi/2$, $t = \pi$ and $t = 3\pi/2$. In Fig. 14 we
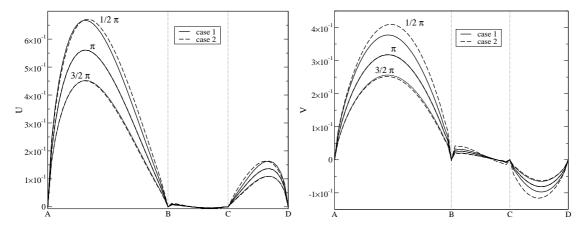
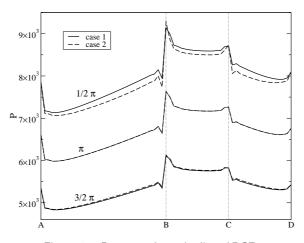Figure 13: u component (left) and v component (right) along the line $ABCD$.

Figure 14: Pressure along the line $ABCD$.

plot the pressure p along the line $ABCD$. We remark that the presence of the deformed body changes the velocity profile due to its expansions and contractions even at this low Reynolds numbers. If the Reynolds number were increased than the change becomes more and more remarkable.

4.4   Large deformation membrane fluid-structure interaction

We now test the proposed domain decomposition methodology for a fully-coupled fluid-structure interaction (FSI) problem, where different subdomains are subjected to different physical laws and compatibility conditions are enforced on the common interface. Note that a fully coupled FSI means that the response of the solid is strongly affected by the response of the fluid, and vice versa and hence we employ a monolithic approach.

In this experiment, we consider a large deformation membrane test that was recently
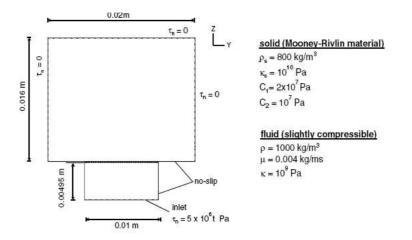
Figure 15: Model dimensions and boundary conditions, solid and fluid properties.

proposed [3] as benchmark test for FSI. Fig. 15 shows the problem considered where two fluid regions are separated by a slightly compressible membrane of thickness $5 \times 10^{-5}m$ Time dependent pressure boundary condition, $\tau_n = 5. \times 10^6 t Pa.$, is considered on the bottom edge of the lower fluid domain. The membrane is considered clamped on the left and right extrema. All the remaining boundary conditions are shown in Fig. 15 together with the fluid and solid properties. In the solid region the following plain stress equilibrium equation is considered

$$\rho_s \ddot{w} - \nabla \cdot \sigma = 0 \quad \text{in } \Omega_s \times (0, T), \tag{4.3}$$

where w is the displacement. The stress tensor σ depends upon left Cauchy-Green tensor B [13] by the following equation

$$\sigma = -\tilde{p} I + 2c_1 B - 2c_2 B^{-1}. \tag{4.4}$$

The left Cauchy-Green tensor is defined as $B = FF^T$ where the F is deformation gradient tensor given by $F = I + \nabla w$. Also, in (4.4) $\tilde{p}$ represents the Lagrange multiplier due to the incompressibility of the solid, $\nabla \cdot w = 0$, and can be considered analogous to the pressure in the fluid flow equation. The momentum equations of the fluid and the solid are coupled on the common interface Γ_{fs} through the compatibility condition between the fluid flow velocity and the solid displacement

$$\dot{w} = u \quad \text{on } \Gamma_{fs} \tag{4.5}$$

and the force equilibrium

$$\lambda_{sf} = -\tau_{fs} \quad \text{on } \Gamma_{fs}. \tag{4.6}$$

Here $\lambda_{sf} = -\sigma \cdot n_{sf}$ represents the force exerted by the fluid on the solid while $\tau_{fs} = -\mu \nabla u \cdot n_{fs} + p n_{sf}$ represents the force exerted by the solid on the fluid; n_{sf} and n_{fs} represent the external normals. The compatibility conditions (4.5) and (4.6) can be used in

equation system (3.1)-(3.4), where different equations for different subdomains should be used. In order to take into account the large deformation of the domain a moving grid is considered in both the fluid and the solid regions via an arbitrary Lagrangian-Eulerian formulation. We solve the transient response with $\Delta t = 0.00005s$ until 0.25. The membrane undergoes under large displacements and large strains. The time history of the coarse mesh is displayed in Fig. 16. The results qualitatively reproduces the results in [3].

Time=0.0   Time=0.10   Time=0.20   Time=0.25
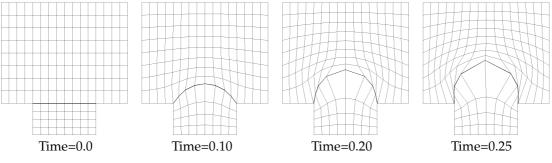
Figure 16: Large deformation membrane test: time histories of the coarse mesh.

Note that this is only a preliminary result and the multilevel algorithm for this application has not been implemented yet. The experiment has been performed to verify that the Vanka-smoother is suitable to solve these applications and can be implemented in an easy and straightforward way. When solving computational blocks inside the fluid domain only the Navier-Stokes equation is considered; and similarly inside the solid domain only the Mooney-Rivlin equation is used. For computational blocks on the boundary the compatibility conditions should be taken into account. When solving boundary blocks in the fluid domain, the time derivative of the solid displacement should be used as Dirichlet boundary condition. When solving boundary blocks in the solid domain, the stress tensor generated from the fluid into the solid should be used as a Neumann non-homogeneous boundary condition. The stress tensor is explicitly evaluated using Eq. (2.14), once again the computational block can be considered as an extended computational block, part in the solid and part in the fluid subdomain with no boundary and this corresponds to an overlapping domain decomposition strategy. We hope to implement the multilevel algorithm discussed for this application and analyze it. This work is in preparation.

5 Conclusion

This paper presents a multilevel domain decomposition technique for solving coupled flow applications. The technique has been employed to numerically simulate four different applications. Note that the focus of the paper was to present the performance of the domain decomposition method presented herein. The four applications presented in this paper provide a good insight and demonstrate the viability of the domain decomposition

technique developed. The numerical studies clearly suggest that by efficiently employing domain decomposition algorithms one can obtain the solution to complex problems with relatively less number of degrees of freedom. These results provide further impetus to examine more complex applications involving flow structure interactions that naturally arise in biological and bio-inspired applications.

Acknowledgments

References

[1] N. Akkas, Aneurysms as a biomechanical instability problem. In Biomechanical Transport Processes (ed. F. Mosora), Plenum Press, 303-311, 1990.

[2] E. Aulisa, S. Manservisi and P. Seshaiyer, A computational multilevel approach for solving 2D Navier-Stokes equations over non-matching grids, Comput. Meth. Appl. Mech. Engrg., 195: 4604-4616, 2006.

[3] K.J. Bathe and G. Ledezma, Benchmark problems for incompressible fluid flows with structural interactions. Computers and Structures, 85: 628-644, 2007.

[4] F.B. Belgacem, L.K. Chilton, P. Seshaiyer, The hp-Mortar FEM for Mixed elasticity and Stokes Problems. Comput. Math. Appl., 46: 35-55, 2003.

[5] C. Bernardi, Y. Maday and A. Patera, Domain decomposition by the mortar element method, Asymptotic and numerical methods for partial differential equation with critical parameters (H.K. et al. eds), Reidel, 269-286, 1993.

[6] J.H. Bramble, Multigrid Methods, 294, Pitman Research Notes in Math, Longman, London, 1993.

[7] S. Canic and D. Mirkovic, A hyperbolic system of conservation laws arising in modeling endovascular treatment of abdominal aortic aneurysm, Hyperbolic Problems: Theory, Numerics, Applications, 141(1): 227-236, 2000.

[8] A. F. Corno, M. Prosi, P. Fridez, P. Zunino, A. Quarteroni and L.K. von Segesser, The non-circular shape of FLOWATCH-PAB prevents the need for pulmonary artery reconstruction after banding, Eur. J. Cardiothorac. Surg., 29: 93-99, 2006.

[9] Y. Di, R. Li and T. Tang, A general moving mesh framework in 3D and its application for simulating the mixture of multi-phase flows, Commun. Comput. Phys., 3: 582-602, 2008.

[10] S. Dong, G.E. Karniadakis, A. Ekmekci, D. Rockwell, A combined direct numerical simulation particle image velocimetry study of the turbulent near wake, J. Fluid Mech., 569: 185-207, 2006.

[11] M. Fernandez, V. Milisic and A. Quarteroni, Analysis of a geometrical multiscale blood flow model based on the coupling of ODE's and hyperbolic PDE's, SIAM J. on MMS, 4(1): 215-236, 2005

[12] Y.C. Fung, Biomechanics: Mechanical Properties of Living Tissues, Springer Verlag, NY, 1993.

[13] A.E. Green and J.E. Adkins, Large Elastic Deformations, Oxford University Press, Oxford, 1960.

[14] M. Gunzburger and L. H. Hou, Treating inhomogeneous essential boundary conditions in finite element methods and the calculation of boundary stresses, SIAM J. Numer. Anal., 29(2): 390-424, 1992.

[15] M. Gunzburger and S. Manservisi, Analysis and approximation of the velocity tracking problem for Navier-Stokes equations with distributed control, SIAM J. Numer. Anal., 37(5): 1481-1512, 1999.

[16] M. Gunzburger and S. Manservisi, The velocity tracking problem for Navier-Stokes flows with bounded distributed control, SIAM J. Cont. Optim., 37: 1913-1945, 1999.

[17] M. Gunzburger and S. Manservisi, On a shape control problem for the stationary Navier-Stokes equations, Math. Model. Numer. Anal., 34(6): 1233-1258, 2000.

[18] V. Girault and P. Raviart, The Finite Element Method for Navier-Stokes Equations: Theory and Algorithms, Springer, New York, 1986.

[19] R.H.W. Hoppe, Adaptive multigrid and domain decomposition methods in the computation of electromagnetic fields, J. Comput. Appl. Math., 168: 245-254, 2004.

[20] J.D. Humphrey and S.K. Kyriacou, The use of Laplace's equation in aneurysm mechanics, Neurological Research, 18: 204-208, 1996.

[21] V. John, P. Knobloch, G. Matthies, L. Tobiska, Non-nested multi-level solvers for finite element discretisations of mixed problems, Computing, 68: 313-341, 2002.

[22] V. John, A comparison of parallel solvers for the incompressible Navier-Stokes equations, Comput. Visual. Sci., 1(4): 193-200, 1999.

[23] V. John and L. Tobiska, Numerical performance of smoothers in coupled multigrid methods for the parallel solution of the incompressible Navier-Stokes equations, Int. J. Numer. Meth. Fluids, 33: 453-473, 2000.

[24] M. Larin and A. Reusken, A comparative study of efficient iterative solvers for generalized Stokes equations, Numer. Lin. Alg. Appl., 15: 13-34, 2007.

[25] C. Liu, J. Shen, X. Yang, Dynamics of defect motion in nematic liquid crystal flow: modeling and numerical simulation, Commun. Comput. Phys., 2: 1184-1198, 2007.

[26] S. Manservisi, Numerical analysis of Vanka-type solvers for steady Stokes and Navier-Stokes flows, SIAM J. Numer. Anal., 44: 2025-2056, 2006.

[27] M. Schafer and S. Turek, The benchmark problem: flow around a cylinder, in Flow Simulation with High Performance Computers II, (E.H. Hirschel ed.), Vol. 52 of Notes on Numerical Fluid Mechanics, 547, Vieweg 1996.

[28] P. Seshaiyer and J.D. Humphrey, On the protective role of contact constraints in saccular aneurysms, Journal of Biomechanics, 34: 607-612, 2001.

[29] P. Seshaiyer and M. Suri, Uniform hp convergence results for the mortar finite element method, Math. Comp., 69: 521-546, 2000.

[30] P. Seshaiyer and M. Suri, *hp* submeshing via non-conforming finite element methods, Comput. Meth. Appl. Mech. Eng., 189: 1011-1030, 2000.

[31] P. Seshaiyer, F.P.K. Hsu, A.D. Shah, S.K. Kyriacou and J.D. Humphrey, Multiaxial mechanical behavior of human saccular aneurysms, Computer Methods in Biomechanics and Biomedical Engineering, 4: 281-289, 2001.

[32] B. Smith, P. Bjorstad and W. Gropp, Domain Decomposition: Parallel Multilevel Methods for Elliptic Partial Differential Equations, Cambridge University Press, 2004.

[33] Z. Tan, K. M. Lim and B. C. Khoo, An adaptive moving mesh method for two-dimensional incompressible viscous flows, Commun. Comput. Phys. 3: 679-703, 2008.

[34] T. Tang, Moving mesh methods for computational fluid dynamics, Contemporary Mathematics, vol. 383, AMS, 2005.

[35] R. Temam, Navier-Stokes Equation, North-Holland, Amsterdam, 1979.

[36] S. Turek, Efficient Solvers for Incompressible Flow Problems: An Algorithmic and Computational Approach, Vol. 6, Lecture Notes in Comput. Sci. Eng., Springer, 1999.

[37] T. Utsumi, T. Aoki, J. Koga, M. Yamagiwa, Solutions of the 1D coupled nonlinear Schrödinger equations by the CIP-BS method, Commun. Comput. Phys., 1: 261-275, 2006.

[38] S. Vanka, Block-implicit multigrid calculation of two-dimensional recirculation flows, Comput. Meth Appl. Mech. Eng., 59(1): 29-48, 1986.

[39] B.Weir, L.Disney and T.Karrison, Sizes of ruptured and unruptured aneurysms in relation to their sites and the ages of patients, J. of Neurosurgery, 96: 64-70, 2002.

[40] M. Möller, D. Kuzmin, S. Turek, Implicit finite element discretizations based on the flux-corrected transport algorithm, International Journal for Numerical Methods in Fluids, 47: 1197-1203, 2005.